



## 3D printed soft composites with tunable hyperelastic properties

Kimberlee Hughes , B. Arda Gozen <sup>\*</sup>

*Washington State University, School of Mechanical and Materials Engineering, Pullman, WA, 99164, United States*

### ARTICLE INFO

Handling Editor: Dr Uday Vaidya

**Keywords:**

Additive manufacturing  
Direct ink writing  
Fused filament fabrication  
Multi-material 3D printing  
Functionally graded

### ABSTRACT

The ability to precisely control spatially varying mechanical properties of soft materials is an emerging need towards the development of functionally graded biomimetic compliant structures. Multi-material additive manufacturing has proven to be an effective method to achieve this goal, however commonly used methods are expensive and limited in material capabilities. This work presents novel soft composites, consisting of a silicone matrix and thermoplastic elastomer reinforcements, fabricated through low-cost extrusion-based additive manufacturing. A customized 3D printer with direct ink write (DIW) and fused filament fabrication (FFF) capabilities is used to print composites with a sinusoidal reinforcement pattern. This parametric pattern allowed us to quantitatively analyze how the frequency and amplitude parameters influenced the hyperelastic behavior of the composites. Spatially varying hyperelastic property control capability is then demonstrated through spatial variation of reinforcement geometry. Information from these samples is used to develop a method of efficiently modeling the design-property relationships of these composites allowing us to predict hyperelastic behavior based on given design parameters. Finally, the capability of this approach to realize as-designed property variations is evaluated. The presented multi-material composites exhibit a broad range of spatially controllable stiffness and strain hardening behavior, owing to their compliant reinforcements with complex design and their unconventional interfacial nature. This approach opens up possibilities to create soft structures to be used in various applications including soft wearables, flexible electronics and tissue phantoms.

### 1. Introduction

The use of soft engineering materials such as silicones has been gaining traction due to the emergence of technologies such as soft robotics, flexible electronics and presurgical organ models. In these applications, compatibility with soft biological systems and the ability to mimic their functionalities is essential. As these technologies continue to advance, there is a need for further development of soft engineering materials and the properties they can exhibit. Different applications require different mechanical behavior, which introduces the need for engineered materials that can meet such specifications.

The mechanical property spectrum exhibited by biological systems is quite challenging to mimic using the conventional material selection, design, and manufacturing approaches used in engineered products. This is primarily because (1) there is a wide range of properties observed across different biological systems, (2) the mechanical nature of these materials is generally hyperelastic, which is non-linear and more complex compared to conventional engineering materials and (3) the properties within given systems can vary spatially by a significant

amount. Mimicking these complexities requires precise spatial control over the non-linear mechanical properties of materials which poses significant manufacturing challenges. Ultimately, this goal of spatial non-linear mechanical property control requires two capabilities: (1) the ability to create structures that have well-controlled, as-designed non-linear mechanical behavior, and (2) the ability to distribute properties precisely across a given design. In the current state of the art, the key innovations needed to address these challenges lie in the design/manufacturing domain.

Tuning mechanical properties of soft materials has been accomplished through various means, such as altering material composition [1–4] or through combination of a soft matrix and stiff reinforcement [5]. There has also been work in producing structures with graded mechanical properties, highly motivated by the desire to address issues of mechanical incompatibility between soft and rigid materials. These methods primarily involve producing multi-material structures by combining materials with different stiffnesses in a single design with distinct interfaces [6,7], or through the matrix-reinforcement method [8,9] by means of tuning the reinforcement geometry to produce

\* Corresponding author.

E-mail addresses: [kimberlee.hughes@wsu.edu](mailto:kimberlee.hughes@wsu.edu) (K. Hughes), [arda.gozen@wsu.edu](mailto:arda.gozen@wsu.edu) (B.A. Gozen).

spatially graded mechanical properties. Implementation of these approaches in the emerging soft material applications require manufacturing techniques capable of realizing high complexity, particularly to accomplish robust property gradients in a single part. In the current state of the art, the manufacturing methods used in this context include well-established high throughput approaches such as molding [1,3,4,8,9], hot pressing [1,2] and soft lithography [5,6]. These methods are generally limited in geometric complexity and require cumbersome and labor-intensive steps to produce multi-material structures, hindering the rapid advancement of soft material applications.

The emergence of additive manufacturing (AM) or 3D printing has widened the possibilities of property tuning by expanding the range of material options, as well as easily integrating the use of multiple materials in a single structure. The layer-by-layer construction allows for complex geometries to be produced quickly with minimal added effort compared to simple designs. Among the various AM methods, vat photopolymerization is capable of producing these complex parts with high-resolution and speed and has been used to create mechanical property tuned structures through variations in light intensity [10,11], wavelength [12], laser scanning velocity [13], and resin chemistry [14–16]. While these techniques have shown much promise in creating mechanically tuned structures and property gradients, there is still a need for exploring multi-material printing processes. Currently, one of the most common multi-material printing methods for structures with tuned and spatially controlled properties is material jetting, which involves the deposition of photopolymer droplets using an array of printheads [17]. The use of multiple printheads allows for the incorporation of multiple materials with a wide range of properties printed within a single structure. As such, this method can be used to easily create parts with precisely tuned mechanical properties that can span several orders of magnitude within a single structure. While this has been shown to be an effective method in producing mechanically tuned materials and gradients [18–24], the required use of proprietary materials and the high-cost limit accessibility as well as applicability in cases where functionality beyond mechanical property gradients is needed.

An alternative AM approach commonly used in manufacturing of soft structures which can address the cost and material issues with the aforementioned methods is Direct Ink Writing (DIW). This extrusion-based process involves the layer-by-layer deposition of liquid phase material precursors, or inks, in the form of extruded filaments [25]. As one of the most versatile and simple AM methods [26], DIW has been used to manufacture soft and flexible structures consisting of various soft polymers [27,28], polymer composites [29–31], hydrogels [32], and even room temperature liquid metals [33] and ionic liquids [34] which are widely used as components of soft and flexible devices. Furthermore, DIW has the capability to easily integrate multiple materials in a single part through multi-nozzle [35–37] or mixing nozzle [38–42] implementations which have been used to produce structures with property gradients. The materials that can be processed through DIW and can be used robustly as a part of functional soft structures generally are on the high end of the mechanical compliance spectrum, such as soft silicones, gels, liquids etc., which limits the extent of property gradation that can be achieved.

As another highly versatile and low-cost extrusion-based AM method, fused filament fabrication (FFF) is capable of printing thermoplastic polymers within a broad spectrum of mechanical compliance, ranging from rigid plastics to soft thermoplastic elastomers (TPE). This method has been used in conjunction with molding [43] to produce mechanically graded soft structures. Considering the available range of mechanical properties in FFF, the combination of DIW and FFF in a single process can expand material options and therefore broaden the range of achievable mechanical properties in a single structure. However, these two methods print materials with different rheological properties which presents challenges when attempting to integrate them, especially when printing solid materials extruded through FFF on top of gel-like materials extruded with DIW. Current work with these

systems has primarily focused on the development of the printing method [44–46]. More research is needed to realize the manufacturing of more complex multi-material structures combining dissimilar materials. Furthermore, despite the capability of AM to realize highly complex designs that eliminates the design constraints of conventional composites, there is a lack of research effort to elucidate the design-mechanical property relationships for such multi-material structures. Specifically missing for soft structures is research studies on their hyperelastic nature. As most efforts focus on controlling the average compliance of soft structures, engineering of the non-linear strain-dependent variation of their compliance through the complexity capabilities of AM remains an exciting opportunity, which we explore in this study.

In this work, we integrate two extrusion-based methods to realize 3D printing of soft composites with tunable and spatially varying hyperelastic behavior, and to understand design-property relationships for these composites. We print composites with two distinct materials in a matrix-reinforcement configuration, simultaneously using DIW to print a soft silicone matrix and FFF to print a TPE reinforcement, which is printed in a sinusoidal pattern. Fig. 1 provides a graphical summary of this work. The objectives of our study are (1) to establish the DIW and FFF process parameters to robustly generate the desired composite part designs (2) to elucidate how the design parameters (i.e. reinforcement amplitude and phase), influence the hyperelastic nature of the composites through tensile testing and phenomenological modeling of stress-strain behavior, and (3) to investigate spatial control of hyperelastic behavior in the composites through unique sinusoidal reinforcement designs with spatially varying amplitude and frequency. This research introduces the rather unconventional concept of compliant reinforcements with complex shapes and demonstrates its unique effects on the composite properties. The presented method carries the potential to enable low-cost precise manufacturing of complex parts with spatially varying, as-designed, non-linear mechanical properties that can advance many applications utilizing soft engineered materials.

## 2. Materials and methods

### 2.1. Sample design

All sample geometries were designed using SOLIDWORKS 2022. As guided by ASTM D412, rectangular test samples were designed instead of dogbones to allow for a sufficient number of reinforcement patterns to be included in the samples. The sample length and width were selected as 120 mm and 25.4 mm, respectively. Each layer of the samples was designed as a separate solid body as illustrated in Fig. 2A. These bodies were then sliced by assigning the reinforcement material and the silicone to the single perimeter and the infill of the solid body, respectively as shown in the sliced part preview in Fig. 2B. Sinusoidal edges of these solid bodies which define the reinforcement geometries were designed using the equation-driven curve function in SOLIDWORKS and were varied by changing amplitude and wavelength. Five different geometries were designed, the geometric parameters of which can be found in Table 1.

Straight line reinforcements were considered to have both an amplitude and frequency of zero. Plain matrix (non-reinforced) samples were also included for comparison. To ensure enough spacing between individual reinforcements, the number of reinforcements in a single layer was set as 6 for all samples. Each sample included three reinforced layers and three non-reinforced (i.e. pure silicone) layers as shown in Fig. 3. The three reinforced layers were printed at a 180-degree phase shift from each other to ensure separation between reinforcements in the build direction, preventing them from forming a single multi-layer high sinusoidal structure. This is sought after to ensure homogenous distribution of interfacial stresses across the composite.

To reduce edge effects in the reinforcement layers, the spacing between the edge of the structure and the reinforcements was kept

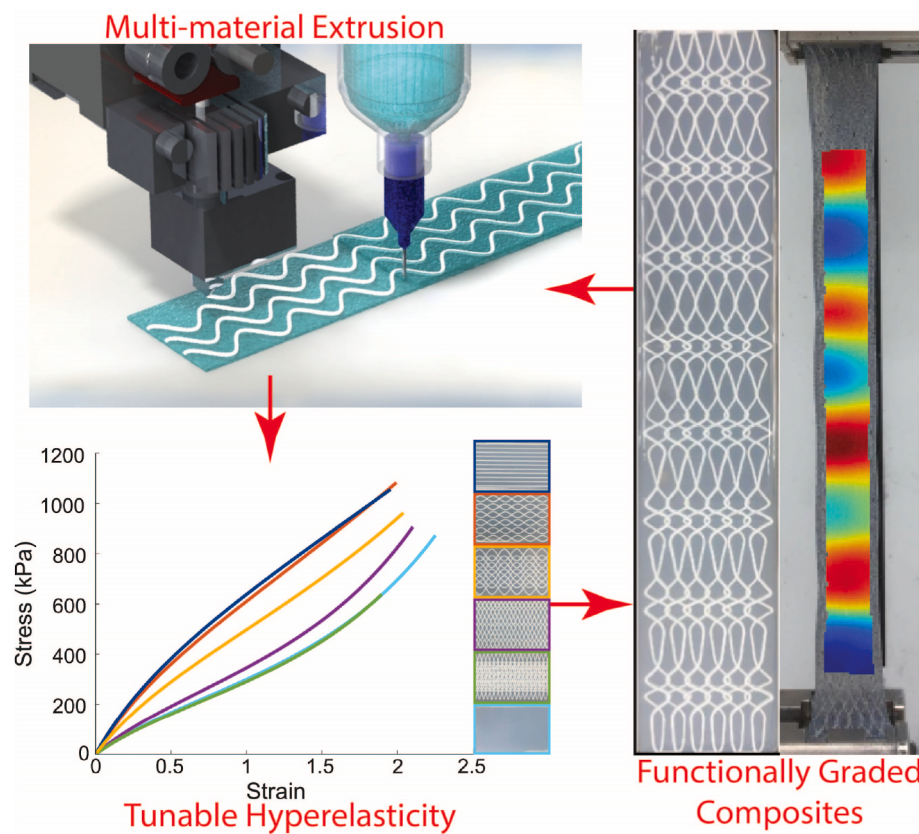


**Fig. 1.** Description of the approach presented in this paper.

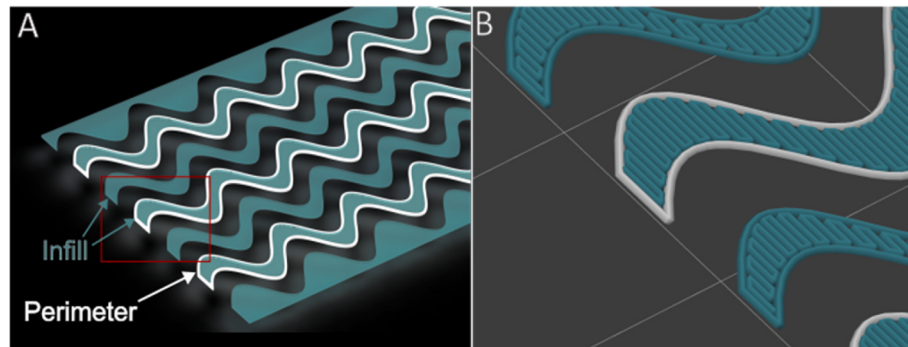


**Fig. 2.** Design of reinforced composite layer. A) Exploded view of single reinforced layer showing separate solid bodies. B) Sliced preview of solid bodies shown in A showing print path. Reinforcements are displayed as white perimeters and silicone is displayed as teal infill.

**Table 1**

Geometric parameters of reinforcements for single frequency/amplitude composites.

Geometry	Frequency [mm <sup>-1</sup> ]	Amplitude [mm]
A	0	0
B	0.5	1.5
C	0.5	3
D	1.5	1.5
E	1.5	3

constant at 1 mm among all the geometries as shown in Fig. S1. Since the width of the sample was also kept constant at 25.4 mm, this meant that the spacing between reinforcements varied between each geometry. Within each structure, however, the spacing between reinforcements was constant.

To demonstrate the capability of spatial mechanical property control, gradient structures were designed. The geometries of the gradient structures had reinforcements with frequency and/or amplitude values that varied as a function of position within each sample as shown in Fig. 4. Because the reinforcements were designed in SOLIDWORKS using the equation-driven curve function, the gradients could be induced by including exponential decay terms into the sine wave equation, as shown in Equations (1)–(3). The coefficients were selected in order to achieve a certain amplitude and frequency range in the graded composites. Three samples were created, one with decaying amplitude, one with decaying frequency, and one with both amplitude and frequency decaying. All methods used to create and test these samples were the same as those used for the constant frequency/amplitude samples.

$$\text{Decaying Amplitude : } y = 3e^{-0.035x} \sin(1.5x + \phi) \quad (1)$$

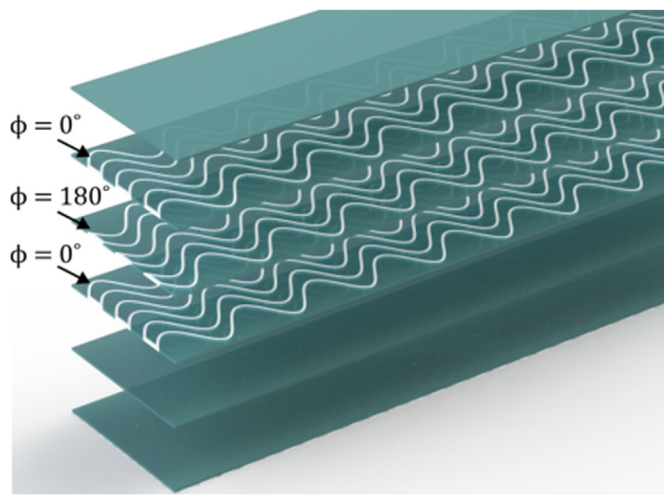


**Fig. 3.** Exploded view of full composite design with three reinforced layers and three non-reinforced layers showing phase shift of middle reinforced layer.

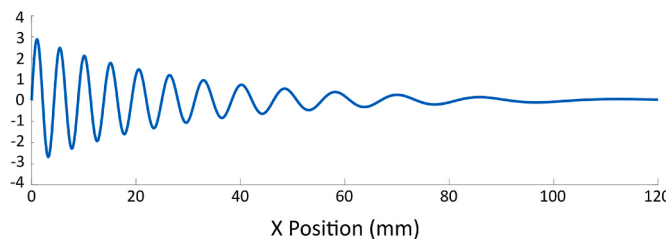


**Fig. 4.** Geometry of a gradient reinforcement with decaying frequency and amplitude as a function of the y-position.

$$\text{Decaying Frequency} : y = 3 \sin(1.5xe^{-0.007x} + \phi) \quad (2)$$

$$\text{Decaying Amplitude and Frequency} : y = 3e^{-0.035x} \sin(1.5xe^{-0.007x} + \phi) \quad (3)$$

## 2.2. Materials

Silicone ink was comprised of a mixture of DOWSIL SE1700 and Smooth-on Ecoflex 00–30. The reinforcement material used was Recreus Filaflex 82A, which is one of the more compliant materials printable with FFF. SE1700 is a high-viscosity silicone that has the proper rheological characteristics necessary for 3D printing, while Ecoflex 00–30 is a highly compliant silicone that has a low viscosity in its uncured state, typically used with molding. These silicones were mixed at a 1:1 ratio to obtain a material significantly softer than the reinforcement while still maintaining the rheological properties conducive to 3D printing as

shown in Fig. 5. Transparent silicones were chosen to be able to clearly evaluate the 3D printed reinforcements. 1-ethynyl-1-cyclohexanol, which served as a cure inhibitor, was added to the silicone mixture at a ratio of  $0.2 \mu\text{L g}^{-1}$  to significantly extend its pot life and enable its printing for long periods. The silicones were mixed in a Thinky AR-100 Planetary Mixer in two stages: first the SE 1700 parts A and B were mixed with the cure inhibitor for 6 min (3 min mixing, 3 min defoaming); next, Ecoflex parts A and B were added and the mixing process was repeated. The silicone ink was then manually loaded into a Nordson EFD 30 cc syringe and centrifuged in a Nordson ProcessMate 5000 centrifuge for 10 min. When not in use, syringes were stored in the refrigerator to further slow curing.

## 2.3. 3D printing

### 2.3.1. 3D printer design

A Qidi Tech X Plus FFF 3D printer was modified to include syringe extrusion capabilities as shown in Fig. S2. Because this printer was designed for a single extruder, the control board was replaced with one that could accommodate extra extruder ports. A Rumba board with three extruder ports was chosen and uploaded with Marlin firmware. The FFF extruder was replaced by a Flexion extruder meant for use with flexible filaments. A custom syringe mount was designed and 3D printed to accommodate two syringes. A Nordson EFD UltimusPlus I pressure dispenser was integrated with the FDM printer through one of the extruder ports on the Rumba using the direction pins, which allowed the dispenser to be turned on or off through the toggling of this direction value. This dispenser was used to print the silicone in the time-pressure mode. The silicone was printed using a Nordson EFD 0.4 mm (22 ga) stainless steel straight nozzle, and a 0.4 mm FFF nozzle was used for the Filaflex printing. A microscope camera was used in conjunction with MATLAB each time the syringe was placed in the mount in order to consistently and precisely determine the offset between the two nozzles. Removable print beds were covered in Kapton tape and coated in Mann Release Technologies Ease Release 2000 mold release for easy removal of cured samples. PrusaSlicer was used to obtain the g-code for the sample, and Repetier Host was used to communicate with the printer.

### 2.3.2. Printing process

Silicone Printing: To account for any day-to-day changes in viscosity of the silicone, the printing pressure was set as constant and the flow rate was measured each day. This was done by performing three 1-min extrusions and measuring the average change in extruded mass. The flow speed was then calculated based on silicone density and nozzle area measurements.

It was determined that success of the reinforcement printing process was significantly sensitive to the height of the pre-deposited silicone layer. As such, it was crucial to achieve the desired layer heights precisely for the first two layers of the structure that consisted solely of silicone. During the printing of silicone, the exact layer height might vary from the prescribed value due to material rheology. In fact, higher

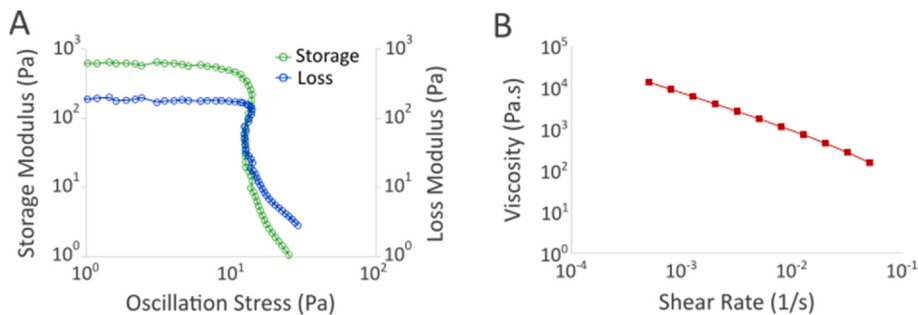


**Fig. 5.** Rheological characterization of uncured silicone matrix material. (A) Results of amplitude sweep denoting yield-stress of about 12 Pa. (B) Results of flow sweep experiment showing shear thinning behavior.

than prescribed layer heights were observed when the flow speed and print speed were matched, which led to failure of the reinforcement printing through submerging of the filaments in the printed silicone. To determine the correct balance between the print and flow speeds, an experimental study was performed where small two-layer test squares were printed, and the sample height was evaluated using a Zygo optical profilometer. By printing these test squares at speeds above and below the calculated flow speed, it was repeatably determined that to achieve the desired layer height, a print speed of 104 % of the flow speed was needed. This was used for all subsequent silicone printing. Details of the experimentation to determine this quantity are provided in Section 3.1.1.

**2.3.2.1. Reinforcement printing.** Preliminary prints showed that using the typical Filaflex print settings did not achieve the desired result when printing on top of uncured silicone. Printing experiments were performed to determine the set of printing parameters, namely print speed, nozzle temperature, and extrusion multiplier, that would produce reinforcements of the desired filament thickness and geometric accuracy. Printing parameters were independently varied, and small test samples were printed to evaluate the effects.

Test samples were designed as four sine wave reinforcements with an amplitude of 1.5 mm and frequency of 1.5 mm<sup>-1</sup> printed on top of a 2-layer silicone rectangle that was 60 mm × 14 mm as shown in Fig. S3. Reinforcements were printed on the uncured silicone samples using varied printing parameters, with speed ranging from 10 mm s<sup>-1</sup> to 40 mm s<sup>-1</sup>, nozzle temperature ranging from 205 °C to 240 °C, and extrusion multiplier ranging from 1.0 to 3.0. Additionally, for each set of printing parameters, a set of reinforcements was printed directly on the print bed for comparison against those printed on silicone. Each print was imaged and processed to identify two quantitative measures of accuracy, one regarding the accuracy of the overall reinforcement pattern and the other regarding the thickness of the reinforcements, which was evaluated against the nozzle diameter of 0.4 mm. To this end, images were processed using MATLAB through grayscale conversion and thresholding to isolate the printed reinforcements, as shown in Fig. 6A–C. Each reinforcement was then broken down into top and bottom boundary arrays using the MATLAB bwboundaries function, and centerline arrays were created using the MATLAB bwskele function as shown in Fig. 6D. The bwboundaries function traces the boundary of an

object and returns an array of pixel locations. The bwskele function uses a process called skeletonization to extract the centerline of an image and returns an array of pixel locations. The filament thickness was measured as the distance between the top and bottom boundaries along the line perpendicular to the centerline at a given point (see Fig. 6E). A thickness value was calculated for each point along the centerline, and all thickness values were then averaged for each reinforcement. An average of the four reinforcements was used for each set of print settings.

For the pattern accuracy evaluation, the goal was to determine the effect of printing parameters on the accuracy of the printed pattern. This was done by comparing the centerline of each printed pattern to the centerline of the target pattern. In order to account for any potential errors involved in the slicing process, the target patterns were taken as those obtained from the slicer preview (as shown in Fig. 6B) instead of the designed sine wave pattern. We quantify the accuracy of the printed patterns through a spatial frequency domain analysis. Here, printed and target patterns are considered as a function of the coordinate  $x$  along the longer length of the samples,  $p(x)$  and  $t(x)$ , respectively. Fourier transforms of these functions were then computed as follows:

$$\mathcal{F}(p(x)) = P(\chi) = P(\chi)e^{j(\chi + \theta_p(\chi))} \quad (4)$$

$$\mathcal{F}(t(x)) = T(\chi) = T(\chi)e^{j(\chi + \theta_t(\chi))} \quad (5)$$

Next, an amplitude error as a function of spatial frequency was calculated as the absolute value of the difference between the amplitudes of the Fourier transforms of the two functions.

$$E(\chi) = |P(\chi) - T(\chi)| \quad (6)$$

Finally, the net pattern error was quantified as the integral of the error function as

$$\bar{E} = \int_0^{X_{max}} E(\chi) d\chi \quad (7)$$

Where  $X_{max}$  is the maximum spatial frequency according to the Nyquist criterion which was 9.81 mm<sup>-1</sup>. The printing temperature, speed and extrusion multiplier used during reinforcement printing were selected to minimize the thickness and pattern error as demonstrated in Section 3.1.2. Additionally, to avoid contact between the heated nozzle and uncured silicone as well as to improve printing of the reinforcements, a

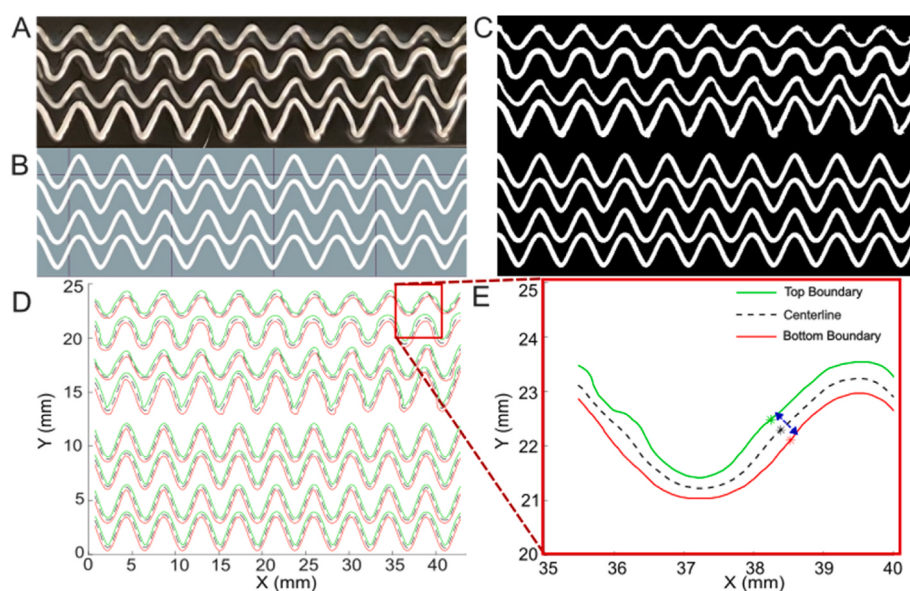


**Fig. 6.** Image processing of printed sinusoidal reinforcements for reinforcement thickness and accuracy calculations. A) Printed test sample. B) Target pattern taken from slicer preview. C) Combined image of A and B after performing grayscale conversion and thresholding using MATLAB. D) Plot of centerlines and top and bottom boundaries of all reinforcements obtained from C. E) Section of D showing points used in reinforcement thickness calculation.

Z-offset of 0.25 mm was manually included in the g-code.

**2.3.2.2. Post processing.** After printing, samples were cured on the removable print bed in a Blue M StabilTherm electric oven at 50 °C for 12 h. In order to prevent the soft samples from slipping out of the test clamps during mechanical testing, acrylic squares were attached to the ends of each sample using Sil-Poxy, a silicone adhesive. After Sil-Poxy application, each sample was set on a hot plate to ensure full curing of the Sil-Poxy.

#### 2.4. Mechanical characterization

Mechanical properties of all cured samples were characterized by a uniaxial tension test using a Mark-10 ESM 303 testing system at a strain rate of 100 mm min<sup>-1</sup>, as guided by ASTM D638. Three samples of each geometry were tested. To obtain accurate stress calculations, precise knowledge of the sample cross-sectional area is required. Due to variations of the printing process, sample thickness (in the build direction) showed variation from the designed dimensions. To precisely measure each sample's thickness, a non-contact laser interferometry method (Keyence LT9031 M) was used.

Digital Image Correlation (DIC) was used to obtain accurate strain measurements. Prior to testing, all samples were painted with black and white spray paint to produce a speckle pattern. This ensured accurate feature recognition within the DIC software. Ncorr [47] a MATLAB-based DIC program, was used for all strain analysis. Videos of all tensile tests were taken with an iPhone 11 camera with a frame rate of 30 fps. Videos were converted to a series of frames, and every tenth frame was input into Ncorr to ensure high strain accuracy while lowering computational load.

### 3. Results

#### 3.1. Additive manufacturing of the composites

##### 3.1.1. Silicone printing

The results of the silicone printing experiments are given in Fig. S4. As noted above, the goal of these tests was to determine what ratio of print speed to flow speed would produce a layer height equal to the nozzle diameter of 0.4 mm, or more specifically that a two-layer silicone structure would have a height of 0.8 mm. 10 mm by 10 mm two-layer silicone squares were printed at varying print speeds on two different days, and optical profilometry images of the prints were obtained as shown in in Fig. S4A. These images were processed to measure their average heights using the pixel statistics as shown in Fig. S4B where the two peaks represent the bottom (substrate) and top surface. The horizontal difference between these peaks provides the average height accordingly. These print heights were plotted against the corresponding Percent Flow Speed of the given day, and a linear fit was applied to each data set (Fig. S4C). Here, flow speed corresponds to the average speed of the ink as it leaves the nozzles and percent flow speed corresponds to the ratio of this speed to the printing speed, which is the speed of the printing nozzle relative to the print bed during the printing operation. Interpolation was then used to determine what Percent Flow Speed would correspond to a height of 0.8 mm. For both data sets, this value came out to be 104 %. This was then confirmed by printing a structure at this print speed, which resulted in a height of 0.8 mm.

##### 3.1.2. Reinforcement printing

As described in Section 2.3.1, test prints were evaluated in terms of printed reinforcement width and pattern accuracy, and resulting reinforcement thicknesses and pattern error values were plotted against varied parameters of speed, extrusion multiplier and nozzle temperature as shown in Fig. S5 to determine the optimal process parameters. Values for reinforcements printed directly on a print bed were determined and

compared with those printed on uncured silicone. In these plots, the data points were determined by averaging the corresponding metric across the four reinforcements printed as shown in the sample pictures given in Figs. S6–S8. The error bars demonstrate the variation of the same metric between those four prints. These results clearly show that the reinforcement printing behavior significantly differed between the bed and silicone prints.

Nozzle temperature appeared to have little effect on the reinforcement thickness in the silicone prints, as seen in Fig. S5A, however it had a strong influence on the pattern accuracy and its variation for the prints on silicone. Following these results, the temperature of 230 °C was chosen for the rest of the studies as it minimizes both the absolute pattern error and its repeatability. The printing speed that resulted in the lowest error for the silicone prints was 25 mm s<sup>-1</sup>, which also yielded one of the smallest thickness variations observed, therefore this speed was used for the rest of the studies. Fig. S5C shows that the extrusion multiplier's effect on reinforcement thickness is significantly smaller for silicone prints than print bed ones. This can be explained by the compliance of the uncured silicone surface which allows for the printed reinforcements to maintain their near-cylindrical shape. The flow rate increase through the increased extrusion multiplier is accordingly reflected on the printed reinforcement diameter in both in-plane and out-of-plane directions. On the other hand, when printed on the rigid print bed, the reinforcement spreads out to a non-cylindrical shape, thus the increasing flow rate primarily affects the line width. When the accuracy results are observed, it can be seen that the pattern error increases considerably for extrusion multipliers over 1.5. We selected an extrusion multiplier value of 1.25 for the rest of the studies, as we have observed better repeatability across various printed samples with this value as compared to an extrusion multiplier of 1.

#### 3.2. Mechanical properties of composite structures

##### 3.2.1. Strain analysis

Ncorr, an open-source MATLAB-based DIC Analysis program, was used for all strain analysis. This program analyzes individual video frames of a sample undergoing deformation and calculates a strain field for a specified region of interest in each frame. For our experiments, this region of interest was selected as the center portion of the sample being tested. For each pixel of each frame, this program outputs the 2-dimensional Green-Lagrangian strain components,  $e_{xx}$ ,  $e_{xy}$  and  $e_{yy}$ , which can then be used to calculate the overall strain of each frame as follows:

$$\varepsilon = \sqrt{2\bar{e}_{yy}} + 1 - 1 \quad (8)$$

Where  $\bar{e}_{yy}$  is the average  $e_{yy}$  value calculated across all pixels in the region of interest for a given video frame.

##### 3.2.2. Hyperelastic modeling

To further understand the behavior of these composites quantitatively, a hyperelastic model was fitted to the experimental data. For this, the Arruda-Boyce [48] model was chosen. This is a commonly used mechanistic model, which means that the extracted parameters could be related to physical properties. Assuming incompressibility, the model is represented as follows:

$$T_{11} = 2C_1 \left( \lambda_1 - \frac{1}{\lambda_1^2} \right) * \sum_i^5 i \alpha_i \beta^{i-1} I_1^{i-1} \quad (9)$$

where  $T_{11}$  is the engineering stress,  $\lambda_1$  is the stretch in the tested direction, and  $I_1$  is the first invariant of the left Cauchy-Green deformation tensor and is equal to the sum of the squares of a material's principal stretches. These values are obtained from the performed uniaxial tension tests. The value  $\alpha$  is a set of known constants specific to the Arruda-Boyce model.  $C_1$  and  $\beta$  are parameters obtained from the model fitting and correspond to the initial shear modulus and the limiting network

stretch, respectively.

The Arruda-Boyce model was fit to the set of all experimental stress-strain data for each geometry using a least squares approach. From this,  $C_1$  and  $\beta$  values were found for each geometry as shown in Table 2, and the corresponding model fits can be seen in Fig. 7A.

Higher  $C_1$  values generally correspond to higher overall stiffness of the composite. This is to be expected given the definition of  $C_1$  as the initial shear modulus. As seen in Table 2,  $C_1$  increases with decreasing amplitude and frequency of the reinforcements, yielding stiffer composites as the reinforcement geometry approaches that of a straight line.  $\beta$ , the limiting network stretch, is defined as

$$\beta = \frac{1}{\lambda_m^2} \quad (10)$$

where  $\lambda_m$  is the locking stretch which is defined in modeling of polymeric materials as the stretch at which the polymer chains become locked and do not continue to elongate. Above this stretch the material is expected to experience strain hardening. As such, the  $\beta$  term is a measure of the strain at which the strain hardening is exhibited in the tested samples, with higher values corresponding to earlier (i.e. at a lower strain) strain hardening. Looking at Fig. 7A, we can see this behavior is visually expressed as an inflection in the stress-strain curve, especially for lower stiffness samples. This  $\beta$  value decreases with decreasing amplitude and frequency, which is exhibited by this inflection point shifting to a higher strain as the reinforcements approach a straight line.

To further observe the effect of the reinforcements on the overall composite behavior, these results were compared with a more conventional method of controlling material compliance, which is to tune the composition of the silicone matrix. To this end, plain matrix samples (with no reinforcements) were printed at different ratios of silicone components. As previously mentioned, the silicone used for the reinforced samples is a 1:1 mixture of two silicones, one stiffer silicone (SE1700), and one very soft silicone (Ecoflex 00-30). In addition to the 1:1 mixture, samples with a 2:1 and a 3:1 ratio of stiff to soft silicone were also printed and tested. Fig. 7B shows the resulting model fits of these samples next to the reinforced composites for comparison. It can be seen that the 2:1 and 3:1 silicone produced stiffer samples, corresponding to higher  $C_1$  values as seen in Table 2. However, there was little change to the resulting shape of the hyperelastic curve compared to the 1:1 silicone. This lack of shape change with increasing stiffness can also be observed in the  $\beta$  values seen in Table 2, where the trend of stiffer silicones having  $\beta$  values that decrease with increasing stiffness is not present in these materials. In contrast, the addition of reinforcements to the 1:1 silicone not only stiffens the composites with increasing amplitude and frequency, but also alters the shape of the hyperelastic curve with respect to the plain 1:1 silicone. This can be clearly seen when comparing the 3:1 silicone with the low amplitude-low frequency sample. This ability to tune the shape of the curve as well as the stiffness gives an additional degree of control over the behavior of the material. Additionally, looking closer at the shape of curves of the reinforced composites, it appears there is likely a specific amplitude and frequency that would produce a composite with linear elastic behavior, which

**Table 2**

Hyperelastic model parameters of tested composites. Reinforced samples are listed with corresponding frequencies and amplitudes. Plain matrix samples with varying ratios of silicone are also given.

Frequency [mm <sup>-1</sup> ]	Amplitude [mm]	$C_1$	$\beta$
0	0	357.14	0.0213
0.5	1.5	325.62	0.0651
0.5	3	253.68	0.1023
1.5	1.5	154.01	0.1969
1.5	3	128.97	0.2006
1:1 Silicone		135.65	0.1875
2:1 Silicone		177.94	0.1564
3:1 Silicone		267.50	0.2199

exhibits a predictability that is highly desirable in applications such as soft robotics and is rarely observed in highly stretchable materials.

Analysis of composite interfaces and their influence on design-property relationships.

One interesting result of this study is that the hyperelastic behavior of the high frequency, high amplitude sample is nearly identical to that of the unreinforced silicone matrix, even showing slightly lower stiffness. This is a remarkable result and is quite unconventional given that these reinforced samples include the largest volume of reinforcing material. This finding is practically desirable as it enables a smooth and continuous transition between softer composites and unreinforced silicone in samples with graded properties. To better understand the source of this behavior, we closely observed the reinforcement-matrix interface for the high amplitude high frequency reinforcements at the undeformed and deformed states as shown in Fig. 8A. It's clear from the images that the reinforcement separates from the matrix at high strains, likely reducing the stress carried by the reinforcing material, leading to the hyperelastic nature of the composite approaching that of the pure silicone. This unique nature of the composite interfaces, which would likely be considered an issue in conventional composites contexts, actually enables a larger mechanical property range in this work.

To further analyze the influence of the reinforcement-matrix interface, we printed two samples by using DIW-printed SE1700 as the reinforcement instead of Filaflex. These samples included sinusoidal reinforcements 0.5 mm<sup>-1</sup> frequency and 1.5 mm amplitude; and 1.5 mm<sup>-1</sup> frequency and 3 mm amplitude. Since SE1700 is one of the constituents of the matrix, we have compatible interfaces even for the high frequency high amplitude sample as shown in Fig. 8A (blue coloring added to SE1700 reinforcement ink for improved visibility). When the hyperelastic characteristics are analyzed, the high frequency, high amplitude sample exhibits slightly stiffer behavior than the plain silicone and high frequency high amplitude Filaflex reinforced sample. Considering the fact that the hardness of SE1700 (Shore 42A) is substantially lower than Filaflex (Shore 80A), this result clearly indicates the effect of the incompatible Filaflex-silicone interface on the high compliance observed at high frequency high amplitude samples. Low frequency, low amplitude sample with SE1700 reinforcements exhibited only slightly stiffer nature as compared to sample with Filaflex reinforcements, showing that as the interfacial separation reduces with lower frequency lower amplitude reinforcements, the composite behavior is dominated more and more by the mechanical properties of the reinforcement.

### 3.3. Functionally graded composites

To see how this modeling approach relates to varying hyperelastic behavior, we analyzed the functionally graded composites described in Section 2.2. A picture of a printed composite is shown in Fig. 9A, and Fig. 9B shows the variation of strain with position on these samples during the tensile test. As shown, the strain at constant stress varies with position in accordance with the results presented in Section 3.2, where increasing frequency and/or amplitude leads to increased compliance within a single part. To further investigate the frequency and amplitude dependence of the hyperelastic properties within a single part, we performed a spatially varying stress-strain analysis. Since the strain results obtained from the DIC analysis provides strain values for every pixel within the region of interest, these values could be used to calculate an average strain for any given discrete y-position along the sample. This could be done for every frame throughout the tensile test, yielding stress-strain curves for each y-position (see Fig. S9).

Further, Equations (1)–(3) outline the spatial frequency and amplitude variation of the reinforcement design, allowing us to assign a corresponding frequency and amplitude value to each stress-strain curve obtained. Three of these curves were identified to have corresponding frequency and amplitude values very close to those of the single frequency/amplitude samples listed in Table 1. The associated stress-strain

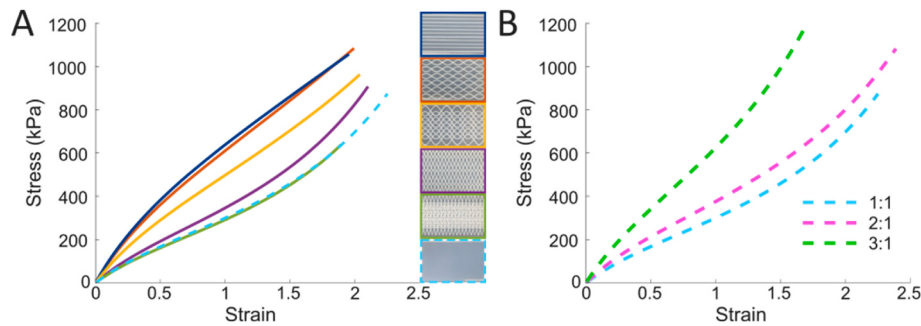


**Fig. 7.** Hyperelastic model fits of A) reinforced single frequency/amplitude composites and B) plain matrix samples at varying silicone ratios.

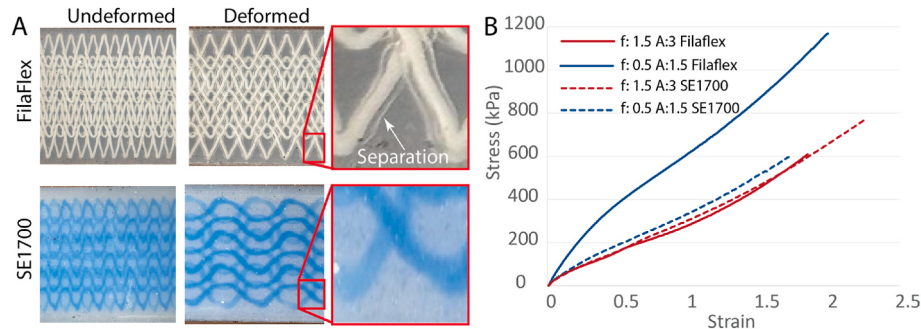


**Fig. 8.** Results of the interface analysis A) Close up images of the deformed and undeformed states of f:1.5 A:3 samples with two different reinforcement materials, B) Stress-strain curves of different Filaflex and SE1700 reinforced composites.

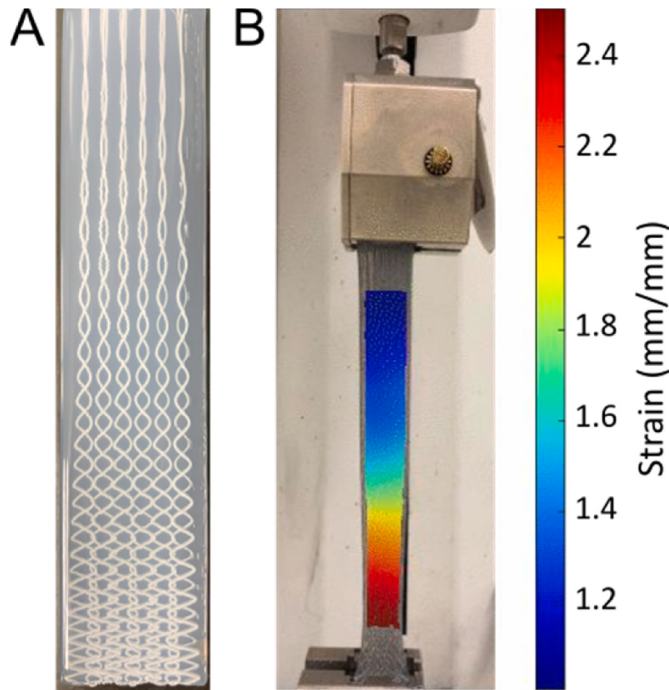


**Fig. 9.** Functionally graded composite. A) Picture of 3D printed composite with reinforcement geometry where frequency and amplitude of the reinforcement are decaying with position. B) Strain variation of graded composite during uniaxial tension test showing how strain varies with reinforcement geometry.

curves were plotted together in Fig. 10 and the results of the model fitting for these curves are given in Table 3. The close agreement between these curves suggests that the frequency and amplitude dependent hyperelastic properties can be thought to be spatially superimposed

in samples with varying amplitude and frequencies, with decent accuracy.

This finding can be utilized to efficiently derive the direct correlations between the design parameters, amplitude and frequency, and the hyperelastic model parameters,  $C_1$  and  $\beta$ , by simply extracting a large number of stress-strain curves from different locations within these graded samples, rather than testing each amplitude and frequency in a dedicated sample. The quantitative design property relationships that correlate  $C_1$  and  $\beta$  to  $f$  and  $A$  can then be used for the direct design of property variations in 3D printed samples. To test this hypothesis, we fit all the stress-strain curves extracted from the graded samples with the Arruda-Boyce model and combined the associated  $C_1$  and  $\beta$  values with those obtained from the constant amplitude/frequency samples to form a large characterization data set. Stepwise regression was then performed on this data set to obtain functional relationships describing  $C_1$  and  $\beta$ , as functions of amplitude and frequency. For the graded samples, the frequency and amplitude values corresponding to each location can be deduced through Equations (1)–(3) yielding the following correlation functions:

$$C_1(f, A) = 22.28*(f(x))^2 - 113.58*f(x) - 9.77*f(x)A(x) - 111.76*A(x) + 15.87*(A(x))^2 + 443.04 \quad (11)$$

$$\beta(f, A) = 0.0859*(f(x))^2 - 0.1237*f(x) - 0.0076*f(x)A(x) - 0.1908*A(x) - 0.0247*(A(x))^2 + 0.041 \quad (12)$$

To test the accuracy of these equations, we first utilized them to predict the spatial strain variation of the graded samples themselves at three different points in time and thus under different axial stresses. We then compared these variations with the ones calculated through the Arruda Boyce model where the strain prediction at each location under a given stress is calculated using the  $C_1$  and  $\beta$  for the corresponding location given by Equations (11) and (12). Results of this analysis are shown in Fig. 11 which demonstrates that the strain predictions closely

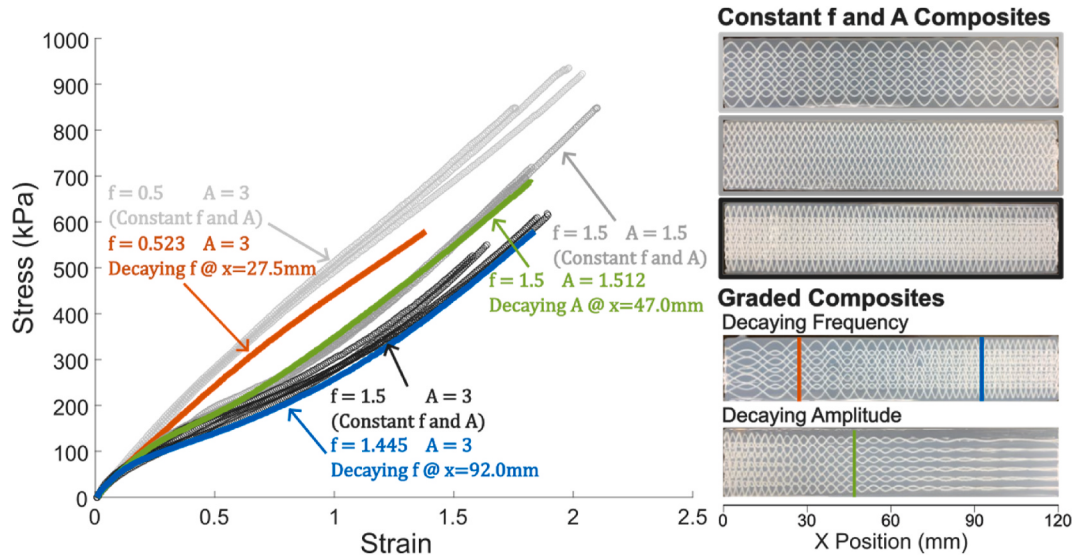


**Fig. 10.** Stress-strain plots of three constant frequency/amplitude composites and three points along the graded composites with corresponding geometries.

**Table 3**

Comparison of geometric and hyperelastic parameters for three single amplitude/frequency composites, and for the points on the graded composites with corresponding geometric parameters.

Sample Type	Frequency [mm <sup>-1</sup> ]	Amplitude [mm]	C <sub>1</sub>	β
Constant f/A	0.5	3	253.68	0.1023
Decaying f @ x = 27.5 mm	0.523	3	202.17	0.1664
Constant f/A	1.5	1.5	154.01	0.1969
Decaying A @ x = 47.0 mm	1.5	1.512	156.03	0.194
Constant f/A	1.5	3	128.97	0.2006
Decaying f @ x = 92.0 mm	1.445	3	110.32	0.2331

**Table 4**  
Design parameters for composites with as-designed properties.

Sample #	A <sub>C<sub>1</sub></sub>	A <sub>β</sub>	O <sub>C<sub>1</sub></sub>	O <sub>β</sub>	Λ [mm]
1	170	-0.12	235	0.16	2.5
2	170	-0.12	235	0.16	5
3	170	-0.12	235	0.16	10
4	130	0	225	0.21	5
5	0	0.15	250	0.175	5

follow the experimental data, thus supporting our initial hypothesis.

As the next step, we evaluated our capability of designing property variations through the use of Equations (11) and (12). To this end, sinusoidal variations of C<sub>1</sub> and β were designed using the following equations.

$$C_1(x) = A_{C_1} \sin\left(\frac{2\pi}{\Lambda}x\right) + O_{C_1} \quad (13) \quad \beta(x) = A_\beta \sin\left(\frac{2\pi}{\Lambda}x\right) + O_\beta \quad (14)$$

Where A<sub>C<sub>1</sub></sub> and A<sub>β</sub> are the amplitude, and O<sub>C<sub>1</sub></sub> and O<sub>β</sub> are the offset of C<sub>1</sub> and β spatial property variations, respectively. Λ is the spatial wavelength of this design in mm. A total of five designs were considered as shown in Table 4.

With C<sub>1</sub> and β defined along the sample length, we could then use Equations (11) and (12) to solve for reinforcement frequency and amplitude at each point to obtain an amplitude and frequency modulated reinforcement design. Accordingly, the reinforcement pattern is given by the following equation:

$$y(x) = A(x) \sin\left(\int_0^x f(x) dx\right) \quad (15)$$

These reinforcement profiles were exported to SOLIDWORKS and then printed as shown in Fig. 12. By analyzing the samples using the method described above, an experimental C<sub>1</sub> and β value could be determined for each position along these samples and compared to the prescribed values, as shown in Fig. 13.

These results show that the presented design approach exhibited decent success in realizing the desired C<sub>1</sub> variations for samples with sufficiently low spatial variation frequencies (e.g. samples 2 and 3). As demonstrated in the results for samples 1 and 2, the accuracy of the method decreases with increasing spatial property variation frequency, indicating that the presented approach has a certain “design bandwidth” for spatial property variation frequency, beyond which it is ineffective. Despite the fact that the proposed approach was able to generate spatial variations with desired spatial frequencies for samples 1–3, capturing the desired β variation amplitudes generally proved challenging, particularly at low β levels. It can also be observed that the accuracies of samples 4 and 5 are significantly lower compared to the first three. In fact, near-sinusoidal variations were observed for β and C<sub>1</sub> in samples 4 and 5, respectively, even though these variables were designed to be constant across the length of the samples.

The particular lack of performance regarding the low β values could be related to the strain range that was captured during these experiments. As described in Section 3.2, low β values represent strain hardening behavior at high strain levels, demonstrated by the inflection in the stress-strain curve. During the testing, our samples failed within the 1.75–2.25 strain range which could be too small to capture the behavior represented by lower beta values. The failure of the method to capture the desired behavior in samples 4 and 5 indicates a fundamental relationship between the two variables in this modeling framework. As demonstrated in Fig. 13, the sinusoidal variation of β in sample 4 and C<sub>1</sub> in sample 5 exhibit the same spatial frequency of C<sub>1</sub> and β, respectively. As also demonstrated through the results of section 3.2, this is an inverse relationship where higher C<sub>1</sub> values generally correspond to lower beta values and vice versa. As such, desired property variations that violate this relationship cannot be achieved with this approach and likely are not physically viable. This limitation brings up the question regarding the use of Arruda-Boyce hyperelastic model as the basis in our approach. As noted in section 3.2, the Arruda-Boyce model facilitates physically relevant characterization of these composites. However, other mechanistic or phenomenological models such as Yeoh [49] and Ogden [50]

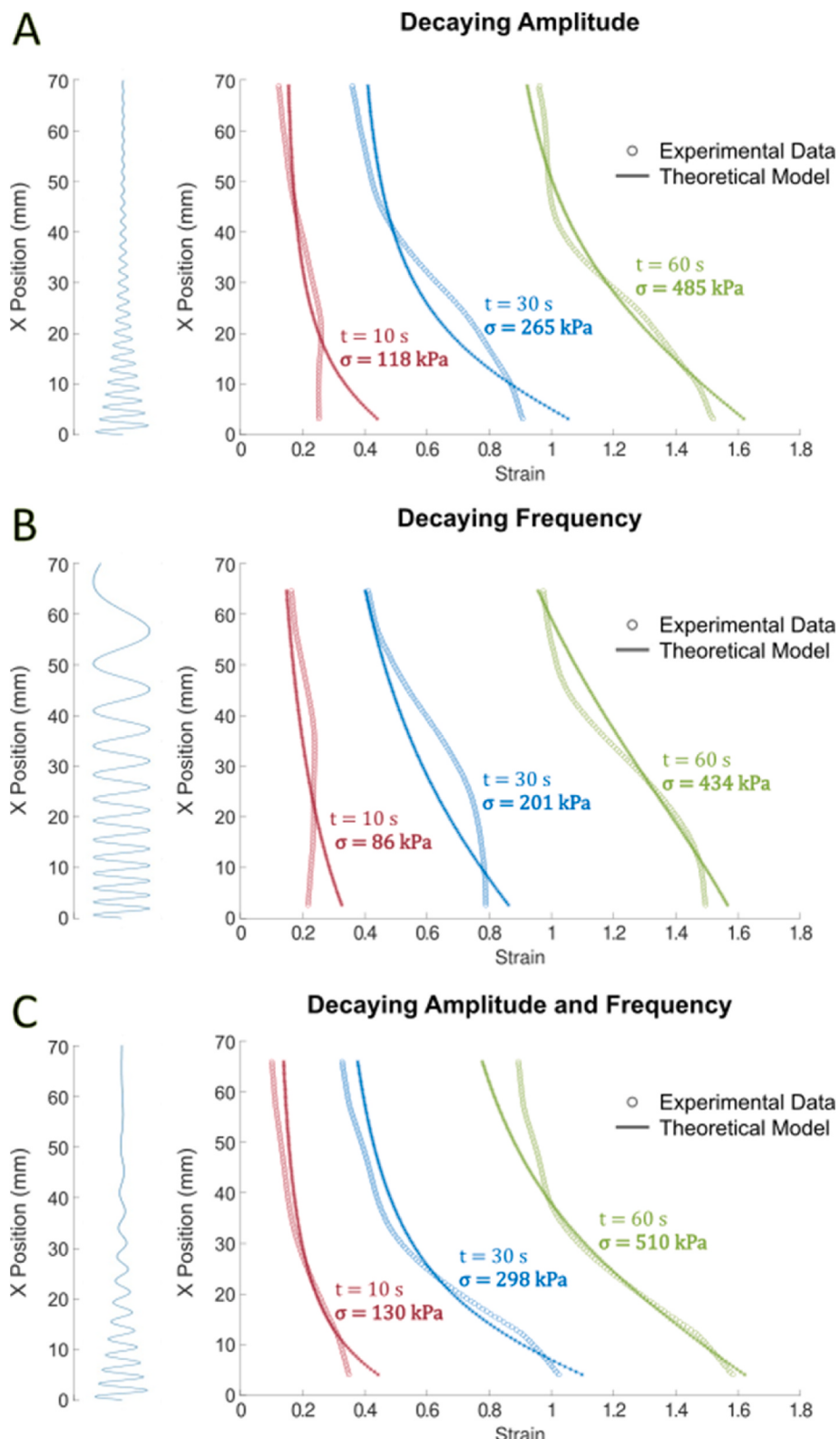


**Fig. 11.** Strain values vs. position along a sample with A) decaying amplitude reinforcement geometry, B) decaying frequency reinforcement geometry, and C) decaying amplitude and frequency reinforcement geometry. A representation of the reinforcement is given on the left in line with the position values. Strain values are given at three different times throughout a uniaxial tension test, which correspond to three different stresses. Experimental values are compared with theoretical values obtained with the model.

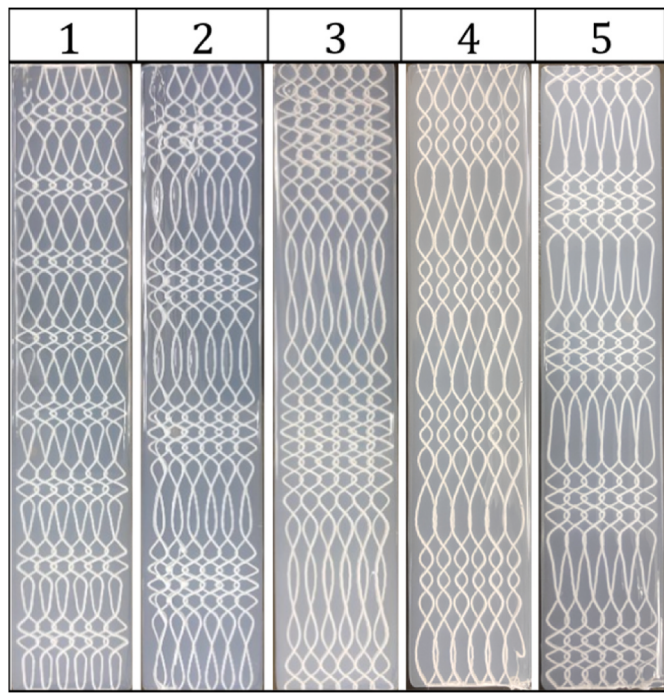


**Fig. 12.** Printed composites with as-designed properties. Numbers correspond to samples listed in Table 4.

could prove more successful for this design framework by providing a higher number of fitting parameters and thus higher degrees of mathematical freedom. Yet, design using such phenomenological models poses a challenge as non-physical fitting parameters are difficult to conceptualize and select for desired mechanical performance. Recent years have seen development of many novel hyperelastic modeling approaches [51], including those integrating emerging artificial intelligence technologies [52,53] with constitutive modeling, which carry a potential to achieve better accuracy if combined with the design approach proposed here.

#### 4. Conclusions and future work

In summary, this paper presents a facile method of additively manufacturing soft multi-material structures with spatially tuned hyperelastic properties. To this end, we integrated two different material extrusion methods into a single system and combined two dissimilar materials in a single structure. With this process we printed composites with complex designs and achieved a high level of accuracy. This allowed us to print multi-material structures with different reinforcement geometries and to investigate how changing the reinforcement geometry leads to different hyperelastic properties. From here, we were able to realize structures with spatially varying hyperelastic behavior through the variation of this geometry within a printed composite. Information obtained from these graded samples led to the development of an efficient method to elucidate the design-property relationships of these composites, which enabled us to predict the stress-strain behavior of a structure given a set of design parameters. Finally, we used this capability to generate composites with as-designed, spatially varying mechanical properties. In its current form, this approach can be used to achieve desired property variations within a limited spatial frequency range.

The novel composites presented in this study introduce a facile, yet advanced approach to generate robust hyperelastic property gradations in soft structures. This advancement is achieved through the unconventional nature of the reinforcements, which are compliant, are integrated in the structures in complex geometries and can deform relative

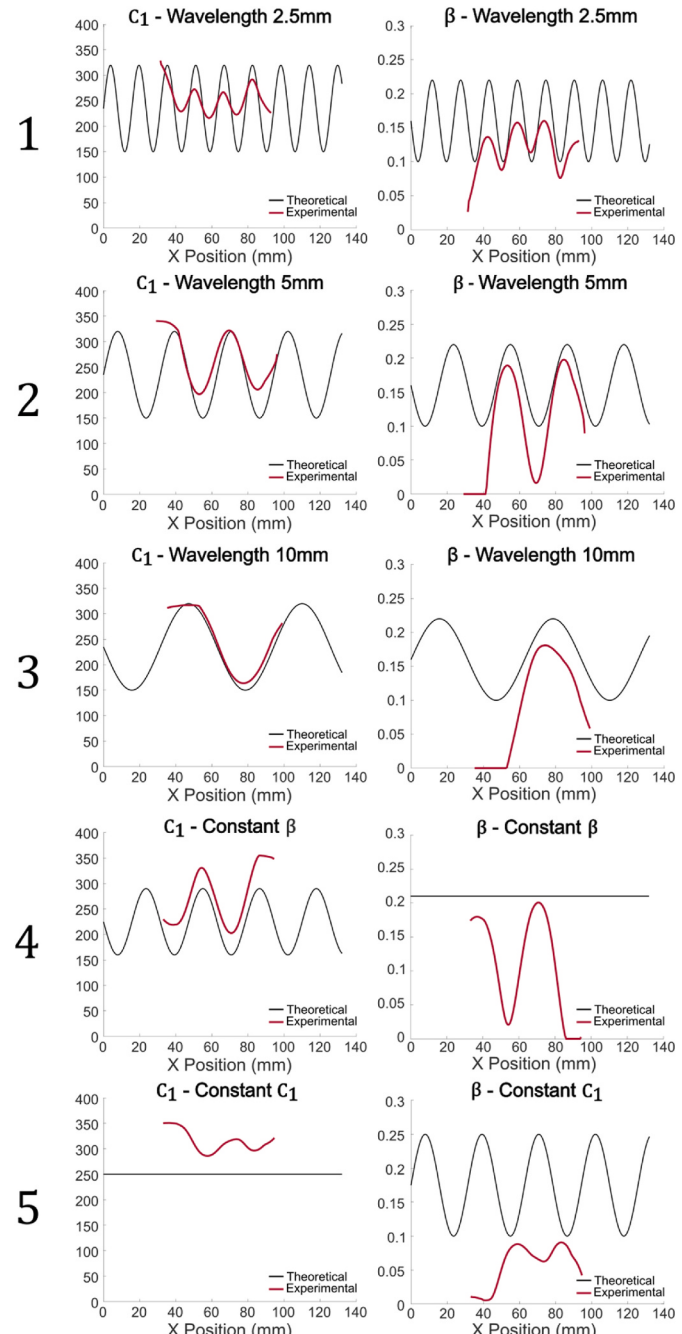


**Fig. 13.**  $C_1$  and  $\beta$  values of composites with as-designed properties. Numbers correspond to samples listed in Table 4.

to the matrix unlike many conventional composites. These properties lead to composites exhibiting nearly identical properties to unreinforced silicone matrix at high spatial frequency and amplitude of the reinforcements, while substantially increasing the stiffness and delaying strain hardening when low spatial frequency and amplitude reinforcements are used. Accordingly, this approach allows for large property gradients with smooth transitions to unreinforced properties, mitigating interfacial issues that are common in such gradated structures. These capabilities yield many opportunities for this technology to advance applications such as soft wearables, flexible electronics and tissue phantoms.

Many opportunities for advancement remain for future work, particularly in studying different reinforcement patterns as well as in material variation. This work focuses on sinusoidal reinforcement

patterns, however more advanced geometries could be used to further explore the capabilities of these composites. Emerging topology optimization approaches [54,55] could be employed in this process to generate more complex designs and achieve a wider range of properties. Additionally, because extrusion-based additive manufacturing methods have high material versatility, there is a large amount of opportunity in exploring different material systems with this method, such as a softer or more rigid reinforcement or matrix materials, or even the combination of multiple reinforcement materials to achieve more complex mechanical behavior. This could even be expanded to the inclusion of liquid reinforcements for the purpose of tuning viscoelastic behavior, which is another major complexity of soft biological materials that is difficult to capture with engineered materials. Finally, the modeling approach can be refined to include more sophisticated material models, likely improving the capability of the method to generate more accurate, as-designed property variations.

#### CRediT authorship contribution statement

**Kimberlee Hughes:** Writing – original draft, Validation, Methodology, Investigation, Formal analysis, Data curation, Conceptualization. **B. Arda Gozen:** Writing – original draft, Supervision, Resources, Project administration, Methodology, Investigation, Conceptualization.

#### Declaration of competing interest

The authors declare the following financial interests/personal relationships which may be considered as potential competing interests:

Kimberlee Hughes reports financial support was provided by National Science Foundation. If there are other authors, they declare that they have no known competing financial interests or personal relationships that could have appeared to influence the work reported in this paper.

#### Acknowledgements

This work was financially supported by the National Science Foundation Graduate Research Fellowship Award 2235552.

#### Appendix A. Supplementary data

Supplementary data to this article can be found online at <https://doi.org/10.1016/j.compositesb.2025.112248>.

#### Data availability

Data will be made available on request.

#### References

- [1] Nasab AM, Sharifi S, Chen S, Jiao Y, Shan W. Robust three-component elastomer–particle–fiber composites with tunable properties for soft robotics. *Adv Intelligent Syst* 2021;3:2000166. <https://doi.org/10.1002/AISY.202000166>.
- [2] Cao P-F, Li B, Hong T, Townsend J, Qiang Z, Xing K, et al. Superstretchable, self-healing polymeric elastomers with tunable properties self-healing polymers. *Adv Funct Mater* 2018;28:1800741. <https://doi.org/10.1002/adfm.201800741>.
- [3] Seighir R, Arcott S. Extended PDMS stiffness range for flexible systems. *Sensor Actuator* 2015;230:33–9. <https://doi.org/10.1016/j.sna.2015.04.011>.
- [4] Leem J, Jiang Y, Robinson A, Xia Y, Zheng X. Data-driven approach to tailoring mechanical properties of a soft material. *Adv Funct Mater* 2023;33:2304451. <https://doi.org/10.1002/adfm.202304451>.
- [5] Jang KI, Chung HU, Xu S, Lee CH, Luan H, Jeong J, et al. Soft network composite materials with deterministic and bio-inspired designs. *Nat Commun* 2015;6. <https://doi.org/10.1038/ncomms7566>. 6566–11.
- [6] Ma Y, Pharr M, Wang L, Kim J, Liu Y, Xue Y, et al. Soft elastomers with ionic liquid-filled cavities as strain isolating substrates for wearable electronics. *Small* 2017;13:1602954. <https://doi.org/10.1002/SML.201602954>.
- [7] Naserifar N, LeDuc PR, Fedder GK. Material gradients in stretchable substrates toward integrated electronic functionality. *Adv Mater* 2016;28:3584–91. <https://doi.org/10.1002/ADMA.201505818>.
- [8] Haque ABMT, Hwang D, Bartlett MD. Graded kirigami composites for programmed strain distributions. *Adv Mater Technol* 2022;7:2101241. <https://doi.org/10.1002/ADMT.202101241>.
- [9] Libanori R, Erb RM, Reiser A, Le Ferrand H, Süess MJ, Spolenak R, et al. Stretchable heterogeneous composites with extreme mechanical gradients. *Nat Commun* 2012;3:1265. <https://doi.org/10.1038/ncomms2281>.
- [10] Peterson GI, Schwartz JJ, Zhang D, Weiss BM, Ganter MA, Storti DW, et al. Production of materials with spatially-controlled cross-link density via vat photopolymerization. *ACS Appl Mater Interfaces* 2016;8:29037–43. [https://doi.org/10.1021/ACSM.6B09768\\_SUPPL\\_FILE/AM6B09768\\_SI\\_001.PDF](https://doi.org/10.1021/ACSM.6B09768_SUPPL_FILE/AM6B09768_SI_001.PDF).
- [11] Kuang X, Wu J, Chen K, Zhao Z, Ding Z, Hu F, et al. Grayscale digital light processing 3D printing for highly functionally graded materials. *Sci Adv* 2019;5:eav5790. <https://doi.org/10.1126/SCIADEV.AAV5790>.
- [12] Schwartz JJ, Boydston AJ. Multimaterial actinic spatial control 3D and 4D printing. *Nat Commun* 2019;10:791. <https://doi.org/10.1038/s41467-019-08639-7>.
- [13] Ota T, Saito A, Tase T, Sato K, Tanaka M, Yoshida K, et al. 3D printing of tough gels having tunable elastic modulus from the same pre-gel solution. *Macromol Chem Phys* 2019;220:1800498. <https://doi.org/10.1002/MACP.201800498>.
- [14] Zhao T, Yu R, Li S, Li X, Zhang Y, Yang X, et al. Superstretchable and processable silicone elastomers by digital light processing 3D printing. *Appl Mater Inter* 2019;11:14391–8. <https://doi.org/10.1021/acsami.9b03156>.
- [15] Wallin TJ, Simonsen L-E, Pan W, Wang K, Giannelis E, Shepherd RF, et al. 3D printable tough silicone double networks. *Nat Commun* 2020;11:4000. <https://doi.org/10.1038/s41467-020-17816-y>.
- [16] Du K, Basuki J, Glattauer V, Mesnard C, Nguyen AT, Alexander DLJ, et al. Digital light processing 3D printing of PDMS-based soft and elastic materials with tunable mechanical properties. Cite this. *ACS Appl Polym Mater* 2021;2021:3049–59. <https://doi.org/10.1021/acsapm.1c00260>.
- [17] Gülcen O, Günaydin K, Tamer A. The state of the art of material jetting—a critical review. *Polymers* 2021;13:2829. <https://doi.org/10.3390/POLYM13162829>.
- [18] Wang K, Wu C, Qian Z, Zhang C, Wang B, Vanman MA. Dual-material 3D printed metamaterials with tunable mechanical properties for patient-specific tissue-mimicking phantoms. *Addit Manuf* 2016;12:31–7. <https://doi.org/10.1016/J.ADDMA.2016.06.006>.
- [19] Wang D, Dong L, Gu G. 3D printed fractal metamaterials with tunable mechanical properties and shape reconfiguration. *Adv Funct Mater* 2023;33:2208849. <https://doi.org/10.1002/ADFM.202208849>.
- [20] Deng Y, Guo X, Lin Y, Huang Z, Li Y. Dual-phase inspired soft electronic sensors with programmable and tunable mechanical properties. *ACS Nano* 2023;17:6423–34. [https://doi.org/10.1021/ACSNANO.2C11245\\_SUPPL\\_FILE/NN2C11245\\_SI\\_005.PDF](https://doi.org/10.1021/ACSNANO.2C11245_SUPPL_FILE/NN2C11245_SI_005.PDF).
- [21] Bartlett NW, Tolley MT, Overvelde JTB, Weaver JC, Mosadegh B, Bertoldi K, et al. A 3D-printed, functionally graded soft robot powered by combustion. *Science* 2015;349:161–5. [https://doi.org/10.1126/SCIENCE.AAB0129\\_SUPPL\\_FILE/AAB0129S2\\_MP4](https://doi.org/10.1126/SCIENCE.AAB0129_SUPPL_FILE/AAB0129S2_MP4).
- [22] Mirzaali MJ, Cruz Saldívar M, Herranz de la Nava A, Gunashekar D, Nouri-Goushki M, Doubrovski EL, et al. Multi-material 3D printing of functionally graded hierarchical soft-hard composites. *Adv Eng Mater* 2020;22:1901142. <https://doi.org/10.1002/ADEM.201901142>.
- [23] Flores Ituarte I, Boddetti N, Hassanii V, Dunn ML, Rosen DW. Design and additive manufacture of functionally graded structures based on digital materials. *Addit Manuf* 2019;30:100839. <https://doi.org/10.1016/j.addma.2019.100839>.
- [24] Dong L, Wang J, Wang D. Modeling and design of three-dimensional voxel printed lattice metamaterials. *Addit Manuf* 2023;69:103532. <https://doi.org/10.1016/j.addma.2023.103532>.
- [25] Lewis JA. Direct ink writing of 3D functional materials. *Addit Manuf* 2006;16:2193–204. <https://doi.org/10.1002/adfm.200600434>.
- [26] Saadi Ma SR, Maguire A, Pottackal NT, Shahedul Hoque Thakur M, Md Ikram M, John Hart A, et al. Direct ink writing: a 3D printing technology for diverse materials. *Adv Mater* 2022;34:2108855. <https://doi.org/10.1002/ADMA.202108855>.
- [27] Durban MM, Lenhardt JM, Wu AS, Small W, Bryson TM, Perez-Perez L, et al. Custom 3D printable silicones with tunable stiffness. *Macromol Rapid Commun* 2018;39:1700563. <https://doi.org/10.1002/marc.201700563>.
- [28] Qiu K, Zhao Z, Haghiashtiani G, Guo SZ, He M, Su R, et al. 3D printed organ models with physical properties of tissue and integrated sensors. *Adv Mater Technol* 2018;3:1700235. <https://doi.org/10.1002/ADMT.201700235>.
- [29] Nesaei S, Rock M, Wang Y, Kessler MR, Gozen A. Additive manufacturing with conductive, viscoelastic polymer composites: direct-ink-writing of electrolytic and anodic poly(ethylene oxide) composites. *Int J Manuf Sci Eng Transa* 2017;139:111004. <https://doi.org/10.1115/1.4037238/383954>.
- [30] Tandel R, Gozen BA. Direct-Ink-writing of liquid metal-graphene-based polymer composites: composition-processing-property relationships. *J Mater Process Technol* 2022;302:117470. <https://doi.org/10.1016/j.jmatprote.2021.117470>.
- [31] Liu W, Peeke LM, Periyasamy M, Campbell RR, Hickner MA. Additive manufacturing of silicone composite structures with continuous carbon fiber reinforcement. *Polym Eng Sci* 2023;63:1716–24. <https://doi.org/10.1002/PEN.26318>.
- [32] Amr M, Dykes I, Counts M, Kernan J, Mallah A, Mendenhall J, et al. 3D printed, mechanically tunable, composite sodium alginate, gelatin and Gum Arabic (SA-GEL-GA) scaffolds. *Bioprinting* 2021;22:e00133. <https://doi.org/10.1016/j.bioprint.2021.e00133>.
- [33] Gannarapu A, Gozen BA. Micro-extrusion-based additive manufacturing with liquid metals and alloys: flow and deposition driven by oxide skin mechanics. *Extreme Mech Lett* 2019;33:100554. <https://doi.org/10.1016/j.eml.2019.100554>.

- [34] Shin H-S, Kim T, Bergbreiter S, Park Y-L. Biomimetic soft airflow sensor with printed ionogel conductor. In: 2nd IEEE international conference on soft robotics, seoul, korea; 2019.
- [35] Zhou Q, Gardea F, Sang Z, Lee S, Pharr M, Sukhishvili SA. A tailororable family of elastomeric-to-rigid, 3D printable, interbonding polymer networks. *Adv Funct Mater* 2020;30. <https://doi.org/10.1002/ADFM.202002374>.
- [36] Lackner F, Knechtli I, Novak M, Nagaraj C, Štiglic AD, Kargl R, et al. 3D-Printed anisotropic nanofiber composites with gradual mechanical properties. *Adv Mater Technol* 2023;8:2201708. <https://doi.org/10.1002/admt.202201708>.
- [37] Joseph VS, Calais T, Stalin T, Jain S, Kumar Thanigaivel N, Sanandiya ND, et al. Silicone/epoxy hybrid resins with tunable mechanical and interfacial properties for additive manufacture of soft robots. *Appl Mater Today* 2021;22:100979. <https://doi.org/10.1016/j.apmt.2021.100979>.
- [38] Kokkinis D, Bouville F, Studdart AR. 3D printing of materials with tunable failure via bioinspired mechanical gradients. *Adv Mater* 2018;30:1705808. <https://doi.org/10.1002/ADMA.201705808>.
- [39] Bakarich SE, Gorkin Iii R, Gately R, Naficy S, In Het Panhuis M, Spinks GM. 3D printing of tough hydrogel composites with spatially varying materials properties. *Addit Manuf* 2017;14:24–30. <https://doi.org/10.1016/j.addma.2016.12.003>.
- [40] Hassan I, Selvaganapathy R. A microfluidic printhead with integrated hybrid mixing by sequential injection for multimaterial 3D printing. *Addit Manuf* 2022; 50:102559. <https://doi.org/10.1016/j.addma.2021.102559>.
- [41] Giachini PAGS, Gupta SS, Wang W, Wood D, Yunusa M, Baharlou E, et al. Additive manufacturing of cellulose-based materials with continuous, multidirectional stiffness gradients. *Sci Adv* 2020;6:eaay0929.
- [42] Ren L, Song Z, Liu H, Han Q, Zhao C, Derby B, et al. 3D printing of materials with spatially non-linearly varying properties. *Mater Des* 2018;156:470–9. <https://doi.org/10.1016/j.matdes.2018.07.012>.
- [43] Estelle K, Blair D, Evans K, Gozen BA. Manufacturing of smart composites with hyperelastic property gradients and shape memory using fused deposition. *J Manuf Process* 2017;28:500–7. <https://doi.org/10.1016/j.jmapro.2017.04.018>.
- [44] Liu W, Campbell RR, Periyasamy M, Hickner MA. Additive manufacturing of silicone-thermoplastic elastomeric composite architectures. *J Compos Mater* 2022; 56:4409–19. [https://doi.org/10.1177/00219983221131614/ASSET/IMAGES/LARGE/10.1177\\_00219983221131614-FIG11.JPG](https://doi.org/10.1177/00219983221131614/ASSET/IMAGES/LARGE/10.1177_00219983221131614-FIG11.JPG).
- [45] Jaksa L, Pahr D, Kronreif G, Lorenz A. Development of a multi-material 3D printer for functional anatomic models. *Int J Bioprint* 2021;7:420. <https://doi.org/10.18063/ijb.v7i4.420>.
- [46] Roach DJ, Hamel CM, Dunn CK, Johnson MV, Kuang X, Qi HJ. The m4 3D printer: a multi-material multi-method additive manufacturing platform for future 3D printed structures. *Addit Manuf* 2019;29:100819. <https://doi.org/10.1016/j.addma.2019.100819>.
- [47] Blaber J, Adair B, Antoniou A. Ncorr: open-source 2D digital image correlation matlab software. *Exp Mech* 2015. <https://doi.org/10.1007/s11340-015-0009-1>.
- [48] Arruda EM, Boyce MC. A three-dimensional constitutive model for the large stretch behavior of rubber elastic materials. *J Mech Phys Solid* 1993;41:389–412. [https://doi.org/10.1016/0022-5096\(93\)90013-6](https://doi.org/10.1016/0022-5096(93)90013-6).
- [49] Yeoh OH. Characterization of elastic properties of carbon-black-filled rubber vulcanizates. *Rubber Chem Technol* 1990;63:792–805. <https://doi.org/10.5254/1.3538289>.
- [50] Ogden RW. On the overall moduli of non-linear elastic composite materials. *J Mech Phys Solid* 1974;22:541–53. [https://doi.org/10.1016/0022-5096\(74\)90033-7](https://doi.org/10.1016/0022-5096(74)90033-7).
- [51] He H, Zhang Q, Zhang Y, Chen J, Zhang L, Li F. A comparative study of 85 hyperelastic constitutive models for both unfilled rubber and highly filled rubber nanocomposite material. *Nano Mater Sci* 2022;4:64–82. <https://doi.org/10.1016/j.nanoms.2021.07.003>.
- [52] Linden L, Klein DK, Kalina KA, Brummund J, Weeger O, Kästner M. Neural networks meet hyperelasticity: a guide to enforcing physics. *J Mech Phys Solid* 2023;179:105363. <https://doi.org/10.1016/j.jmps.2023.105363>.
- [53] Flaschel M, Yu H, Reiter N, Hinrichsen J, Budday S, Steinmann P, et al. Automated discovery of interpretable hyperelastic material models for human brain tissue with EUCLID. *J Mech Phys Solid* 2023;180:105404. <https://doi.org/10.1016/j.jmps.2023.105404>.
- [54] Liu J, Gaynor AT, Chen S, Kang Z, Suresh K, Takezawa A, et al. Current and future trends in topology optimization for additive manufacturing. *Struct Multidiscip Optim* 2018;57:2457–83. <https://doi.org/10.1007/s00158-018-1994-3>.
- [55] Zhu J, Zhou H, Wang C, Zhou L, Yuan S, Zhang W. A review of topology optimization for additive manufacturing: status and challenges Production and hosting by Elsevier. *Chin J Aeronaut* 2021;34:91–110. <https://doi.org/10.1016/j.cja.2020.09.020>.